International Journal of Remote Sensing

ISSN: (Print) (Online) Journal homepage: https://www.tandfonline.com/loi/tres20

Space target detection in optical image sequences for wide-field surveillance

Dan Liu , Xiaodong Wang , Yunhui Li , Zeming Xu , Jianing Wang & Zhonghui Mao

To cite this article: Dan Liu , Xiaodong Wang , Yunhui Li , Zeming Xu , Jianing Wang & Zhonghui Mao (2020) Space target detection in optical image sequences for wide-field surveillance, International Journal of Remote Sensing, 41:20, 7846-7867, DOI: 10.1080/01431161.2020.1782508

To link to this article: https://doi.org/10.1080/01431161.2020.1782508

INTERNATIONAL JOURNAL OF REMOTE SENSING
2020, VOL. 41, NO. 20, 7846–7867
https://doi.org/10.1080/01431161.2020.1782508

Space target detection in optical image sequences for wide-field surveillance

Dan Liu[a,b], Xiaodong Wang[a], Yunhui Li[a], Zeming Xu[a,b], Jianing Wang[a,b] and Zhonghui Mao[a,b]

[a]Changchun Institute of Optics, Fine Mechanics and Physics, Chinese Academy of Sciences, Changchun, China; [b]University of the Chinese Academy of Sciences, Beijing, China

ABSTRACT

A wide-field surveillance system with a long exposure time has a stronger detection capability for faint space targets. However, some of the complexities it generates also pose difficulties for space target detection; a large amount of image data, numberless object points, some stars manifesting as streak-like sources, and possible discontinuous or nonlinear target trajectories. This paper presents a high precision and low computational-cost space target detection method to overcome these obstacles. Firstly, the minimum external rectangle method is implemented to effectively remove stars and noise. Secondly, the motion velocity of the targets is calculated as the basis for predicting the allowed state transition region in each image of the frame set. Finally, a dynamic programming sliding window method is proposed to detect space targets with continuous, discontinuous, linear or nonlinear trajectories. The experimental results show that this method can effectively detect faint space targets in wide-field surveillance under a long exposure time. This method also has the advantage of a low computational cost.

ARTICLE HISTORY
Received 4 March 2020
Accepted 19 April 2020

1. Introduction

Space targets are mainly satellites and space debris in near-earth space (Mehrholzet, Leushacke, and Flury 2002; Yang and Lin 2010). Since sputnik-1 was launched in 1957 (Castronuovo 2011), the number of space targets has been constantly increasing (Wirnsberger, Baur, and Kirchner 2015; Esmiller et al. 2014). Only a small portion of the detected space targets are active satellites, and the rest can be regarded as space debris; if such a large number of space targets collide with one other, it will pose a remarkable threat to human space activities (Nunez et al. 2015; Li et al. 2019). In order to ensure the safety of the working spacecraft and the normal progress of human space activities, it is necessary to deeply study the detection, warning, protection and other aspects of space targets, and space target detection technology is the basis of the above work. Hence, it is imperative that we can detect space targets. At present, the commonly used space target detection methods include radar detection and photoelectric detection. Although radar

CONTACT Xiaodong Wang ciomp_d@126.com Changchun Institute of Optics, Fine Mechanics and Physics, Chinese Academy of Sciences, Changchun, China

detection can achieve all-weather work, it has poor concealment, high cost, and poor detection accuracy and distance. The photoelectric detection technology is relatively mature, with high accuracy, low cost and low energy consumption. Therefore, this paper uses the photoelectric detection method to detect the space target.

Detection and tracking of faint space targets from optical images is problematic in many wide-field space surveillance applications. Typically, the space targets imaged on the focal plane only cover a small number of pixels, because of their large distance from the charge-coupled device (CCD) sensors. This means the target looks like a point with a low intensity embedded in a strong background clutter (Sease, Flewelling, and Black 2017). Therefore, feature-based methods that perform well in the case of a homogeneous background, such as template matching (Liu et al. 2012, 2013), morphological operators (Bai 2013; Bai et al. 2009; Wei, Xing, and You 2018), and threshold methods (Xu et al. 2013), fail to detect faint space targets in a single frame image. Many methods for detecting faint targets from images with a low signal-to-noise ratio (SNR) have been proposed, especially for applications in infrared surveillance (Gao, Lin, and An 2019; Chen 2019; Dong et al. 2014; Zhang et al. 2018). Reed, Gagliardi, and Stotts (1990) developed the recursive space target detection method based on three-dimensional matched filtering. This method can exhibit a theoretically optimum performance in detecting space targets moving at the same velocity. However, for targets with unknown velocities, the performance of the algorithm was degraded. Chu (1988) proposed a moving target detection algorithm called maximum value projection, which downscales three-dimensional detection into two-dimensional detection to reduce the computation. This method performs 2D velocity-matched filtering to detect the target streak. However, because of velocity mismatch resulting from the partition of the velocity space (Chu 1989), the SNR at the output of the matched filter is reduced.

To solve this problem, a series of methods were proposed. Based on the maximum projection method, Yao et al. (2015) proposed a method to detect space targets and estimate their velocities. Kravchonok (2011) used an improved optical flow method to detect moving objects by judging the change in the optical flow vector in images. Blostein and Huang (1991) proposed a method called multistage hypothesis testing (MHT), which is used to detect faint space targets. In this method, a large number of candidate trajectories are made into a tree structure lookup table. Hypothesis testing is used to delete the structure of each layer, and the unconfirmed trajectories are removed. On this basis, many improved algorithms have been proposed. Blostein and Richardson (1994) proposed the multiple multistage hypothesis test tracking (MMHTT) method to detect faint space targets. This method extends tracks formed from sequentially detected target trajectory segments using a multiple hypothesis tracking strategy. Ahmadi and Salari (2015) proposed a hierarchal tracking system to solve the problem of processing a tree structure with a large number of branches in MHT. Barniv (1985) proposed the Dynamic Programming Algorithm (DPA) which solves the problem of small and dim target trajectory search by segmentation optimization. This method transforms the problem of faint target detection into the problem of finding the line with the largest grey cumulative value in a series of trajectories. Arnold, Shaw, and Pasternack (1993) modified the likelihood function in the recursive equation to a log-likelihood ratio function, therefore enhancing the method to better adapt to the nonlinear noise model. Tonissen et al. (1996) used the sum of the measurements as the optimal value function in order to eliminate the complex transfer function in the recursive process. The DPA is performed in an efficient manner; exhaustive search for all possible space target trajectories (Johnston and Krishnamurthy 2000). However, these algorithms still have some obstacles. Firstly, the computational cost is high (especially in wide-field surveillance), the amount of image data is large, and the number of objects is numerous. Secondly, in the case of a long exposure time, some stars manifest as streak-like sources, background noise increases, and the target trajectory may be discontinuous or nonlinear; resulting in a decrease in the detection performance of the algorithm. The target detection is unsatisfactory.

To overcome these obstacles, we propose a high precision and low computational-cost space target detection method named dynamic programming sliding window method (DPSWM). Firstly, the bright stars and noise are removed by using the proposed minimum external rectangle method. We use the minimum external rectangle method in the time index image instead of the single frame image to increase the difference between motion characteristics of stars and targets, this means that the stars and noise can be filtered from the image as much as possible. The intensities of the stars are estimated to further eliminate them from the image. Secondly, the motion velocity of the targets can be calculated as the basis for predicting the allowed state transition region in each image of the frame set. We only need to search for different orbital altitude targets in the allowed state transition region rather than at every pixel in every sequence image. Therefore, this method can effectively detect space targets with different orbital altitudes and nonlinear trajectories, and significantly save computational cost. Thirdly, the dynamic programming sliding window method is adopted to detect space targets. The forward and reverse bidirectional detection methods ensure the detection probability of discontinuous trajectories.

2. Imaging characteristics

An optical image is modelled as:

$$\mathbf{f}(i,j,k) = \mathbf{B}(i,j,k) + \mathbf{S}(i,j,k) + \mathbf{T}(i,j,k) + \mathbf{n}(i,j,k) \tag{1}$$

where (i,j) denotes the pixel coordinates of the image, k is the frame index, $\mathbf{f}(i,j,k)$ is an $(M \times N)$ greyscale image, M and N represent the number of rows and columns of the image respectively. $\mathbf{B}(i,j,k)$ is the background, $\mathbf{S}(i,j,k)$ is the star, $\mathbf{T}(i,j,k)$ is the target, and $\mathbf{n}(i,j,k)$ is the noise.

2.1. Characteristics of stars

Influenced by the hardware limitation of the sensor and atmospheric interference, the imaging process has the effect of point spread function (PSF) blurring. The grey level of the target decreases gradually from the centre to the surrounding area, which can be fitted to a gaussian function. Assuming that $f(x,y)$ is the intensity of the image at (x,y) and (x_0,y_0) is the target centre, the model is as follows:

$$f(x,y) = A\exp\left\{-\frac{1}{2}\left[\frac{(x-x_0)^2}{{\sigma_x}^2} + \frac{(y-y_0)^2}{{\sigma_y}^2}\right]\right\} \tag{2}$$

where A is the fixed coefficient (the energy of the object imaging in the coordinate (x_0, y_0)), and σ_x and σ_y refer to the horizontal and vertical spread radius of the object, respectively. Ideally, a distant star appears as a symmetrical point source object, i.e. the horizontal spread radius is equal to the vertical spread radius $(\sigma_x = \sigma_y)$ (see Figure 1(a,b)).

2.2. Characteristics of space targets

The space target is very far away from the charge-coupled device (CCD) sensor and can be regarded as a point light source at infinity. Under the conditions of a long exposure time and sidereal tracking mode, the space target image on the focal plane is seen as a streak-like source object, thus the horizontal spread radius is not equal to the vertical spread radius $(\sigma_x \neq \sigma_y)$, Moreover, the motion direction of the space target is random (see Figure 1(c,d)). Typically, the space targets imaged on the focal plane only cover a small number of pixels. For better representation, an angularly related anisotropic gaussian diffusion function is applied to construct a streak-like target imaging model.

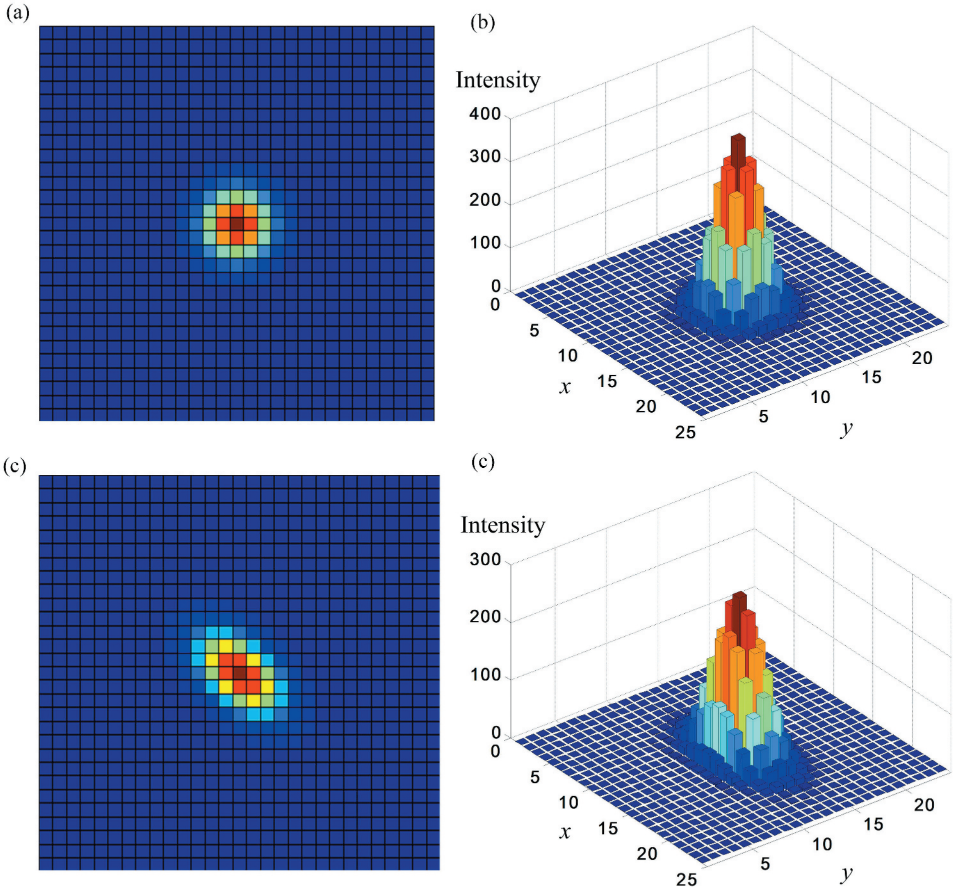

Figure 1. (a) Imaging model of an ideal star; (b) 3D plot of a star; (c) imaging model of a space target; (d) 3D plot of a space target.

$$f(x,y) = A\exp\left\{-\frac{1}{2}\left[\frac{[(x - x_0)\cos\theta + (y - y_0)\sin\theta]^2}{{\sigma_x}^2} + \frac{[(x - x_0)\sin\theta + (y - y_0)\cos\theta]^2}{{\sigma_y}^2}\right]\right\} \tag{3}$$

The orientation parameter θ determining the rotation angle of the target, is defined as the angle that the original coordinate system rotates counterclockwise relative to the new coordinate system (see Figure 2)

3. Star and noise removal

3.1. Principle of a time-index image

Chu (1988) proposed a moving target detection algorithm called maximum value projection. If K frame images are selected to form a frame set, then the maximum

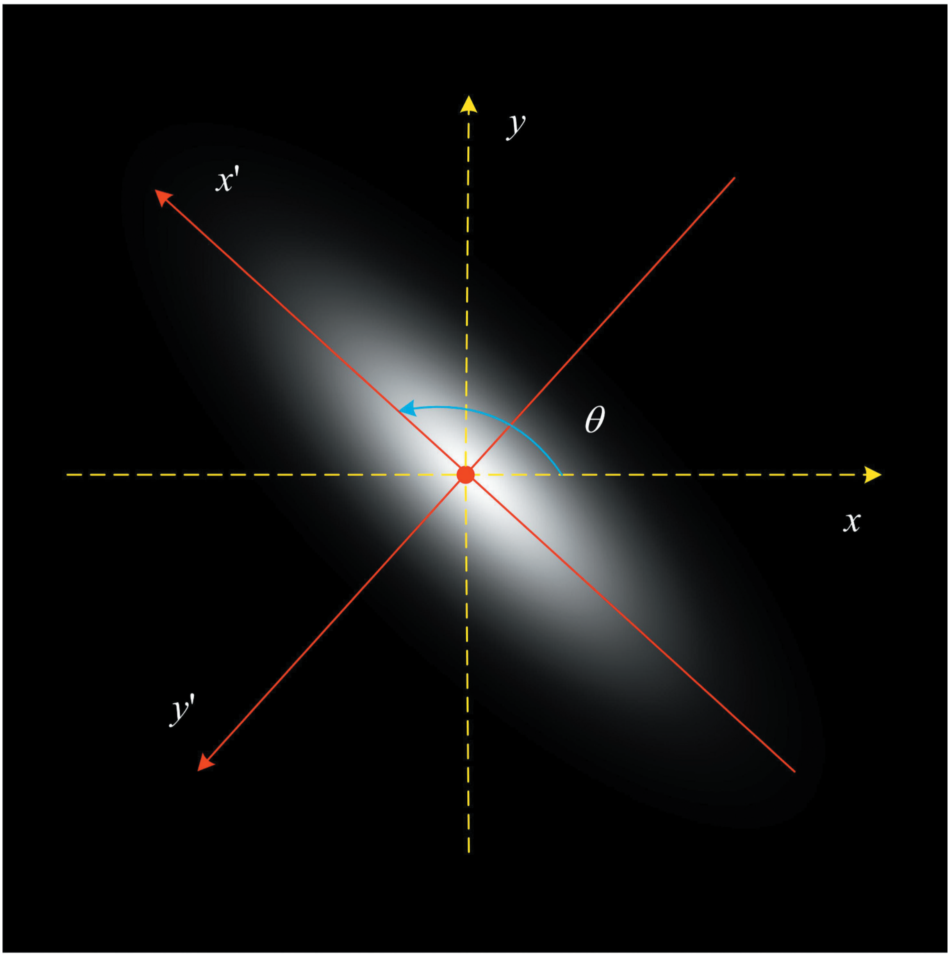

Figure 2. Angle-related imaging model of a space target.

value projection image (maximum image) can be obtained with the following equation.

$$\mathbf{z}(i,j) = \max[\mathbf{f}(i,j,k)](1 \leq k \leq K) \tag{4}$$

where $\mathbf{z}(i,j)$ is the maximum image.

The time-index image can be calculated with Equation (5)

$$\mathbf{z}(i,j) = \mathbf{f}(i,j,k) \Rightarrow \mathbf{t}(i,j) = k \tag{5}$$

where $\mathbf{t}(i,j)$ represents the time-index image. When the maximum image $\mathbf{z}(i,j)$ is equal to $\mathbf{f}(i,j,k)$ at the image coordinates (i,j), the value of $\mathbf{t}(i,j)$ at (i,j) is equal to k; when the same grey value appears at the same coordinates in different images, the smaller frame index is taken.

Subsequently, a binary image, which includes the stars and the space targets, is generated using a threshold $T_{\mathbf{z}}$. The threshold $T_{\mathbf{z}}$ can be estimated using the improved adaptive method (Xi et al. 2016).

$$\mathbf{b}_{\mathbf{z}0}(i,j) = \begin{cases} 0 & \mathbf{z}(i,j) < T_{\mathbf{z}} \\ 1 & \mathbf{z}(i,j) \geq T_{\mathbf{z}} \end{cases} \tag{6}$$

The ‘close’ operation in morphological filtering is applied to eliminate narrow breaks and slender gaps in the binary image by using a flat rectangle-shaped structuring element, $\boldsymbol{\Phi}$. The binary image can then be given by:

$$\mathbf{b}_{\mathbf{z}}(i,j) = \mathbf{b}_{\mathbf{z}0}(i,j) \cdot \boldsymbol{\Phi} \tag{7}$$

where $\cdot$ is the ‘close’ operation in morphological filtering.

3.2. Star and noise removal using the minimum external rectangle method

According to the characteristics of stars and space targets, stars are symmetrically distributed, and space targets are strip-shaped. Therefore, there is a difference in the aspect ratio of the minimum external rectangle between the star and the space target; the minimum external rectangle is calculated in the time-index image composed of two frames in order to increase this difference (see Figure 3). The space targets are roughly extracted by the following characteristics.

$$L = \sqrt{(X_1 - X_2)^2 + (Y_1 - Y_2)^2} \tag{8}$$

$$W = \sqrt{(X_3 - X_2)^2 + (Y_3 - Y_2)^2} \tag{9}$$

$$R = \frac{L}{W} = \frac{\sqrt{(X_1 - X_2)^2 + (Y_1 - Y_2)^2}}{\sqrt{(X_3 - X_2)^2 + (Y_3 - Y_2)^2}} \tag{10}$$

where L and W represent the length and width of the minimum external rectangle, respectively. (X_n,Y_n) are the minimum external rectangle vertex coordinates (n = 1, 2, 3, 4). R is the aspect ratio.

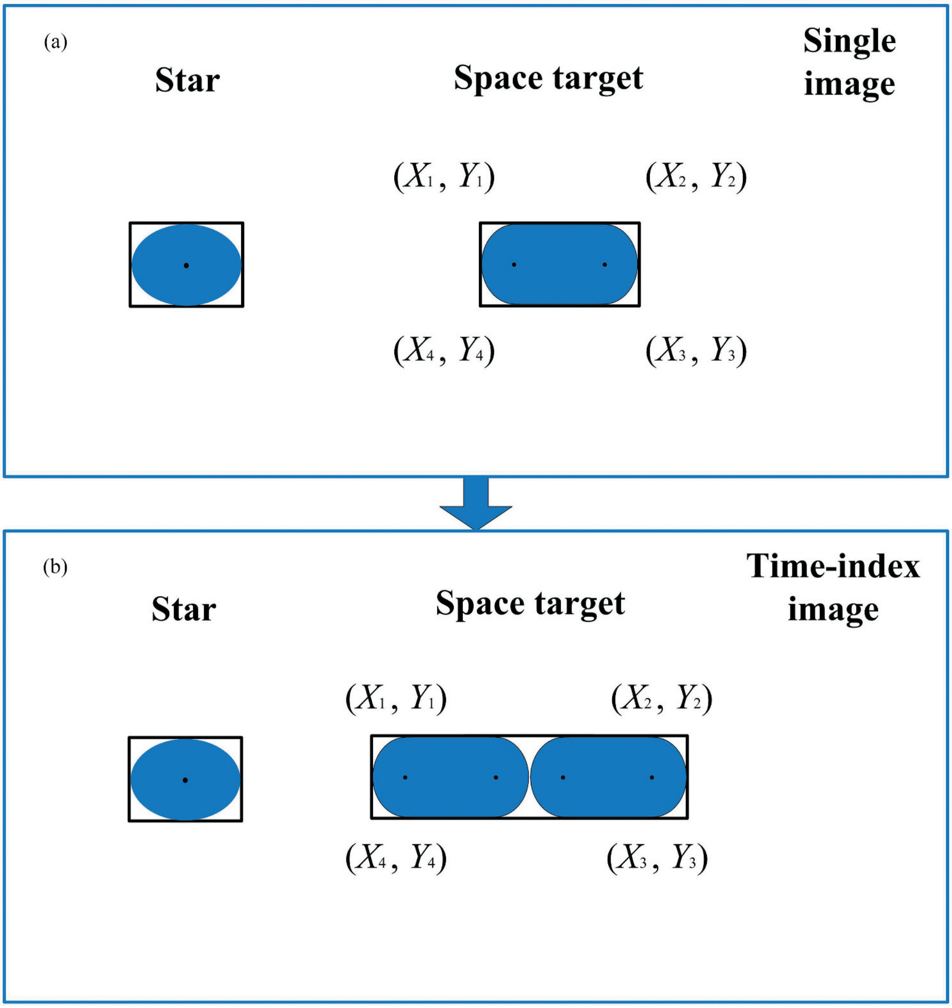

Figure 3. Minimal external rectangle diagrams of space targets and stars: (a) in the single image; (b) in the time-index image.

Then, the image detected by the minimum external rectangle can be obtained using the following formula:

$$\overline{\mathbf{b}_{\mathbf{z}}}(i,j) = \begin{cases} 0 & R < R_{\mathrm{th}} \\ \mathbf{b}_{\mathbf{z}}(i,j) & R \geq R_{\mathrm{th}} \end{cases} \tag{11}$$

where R_{th} represents the minimum external rectangle aspect ratio threshold. A low threshold classifies more connected areas into space targets, which introduces more false alarms. A high threshold significantly reduces the number of false alarms, but introduces more missing space targets. In order to solve these problems, a two-stage detection method is used to improve detection probability. In this section, a low threshold is used to extract candidate targets to ensure detection probability. In the second phase, the false alarms are further removed with strict dynamic programming sliding window conditions. This method reduces the amount of calculation while ensuring the probability of detection.

3.3. Bright star removal

The platform vibration and long exposure time cause the background stars to appear streak-like and the horizontal spread radius of some stars is not equal to the vertical spread radius ($\sigma_x \neq \sigma_y$) (see Figure 4). In this situation, we can also apply the angle-related anisotropic gaussian spread function to construct a streak-like star imaging model.

At this time, the stars cannot be completely removed by the minimum external rectangle method. The key step for removing the stars is to estimate the intensity of the stars and then subtract these from the image. The median filter is used to estimate the intensity. The median filtered image is expressed as follows:

$$\mathbf{m}(i,j) = \mathrm{median}[\mathbf{f}(i,j,k)](1 \le k \le K) \tag{12}$$

In this image, the stars and noise still exist, while the space targets are absent. The stars are removed by subtracting the median image from the maximum image.

$$\bar{\mathbf{z}}(i,j) = \mathbf{z}(\mathrm{i},\mathrm{j}) - \mathbf{m}(\mathrm{i},\mathrm{j}) \tag{13}$$

However, in different images, the noise intensity fluctuates within a certain range, and the effect of these fluctuations is removed by the improved adaptive threshold method (Xi et al. 2016).

$$\mathbf{b}_{\bar{\mathbf{z}}}(i,j) = \begin{cases} 0 & \bar{\mathbf{z}}(i,j) < T_{\bar{\mathbf{z}}} \\ 1 & \bar{\mathbf{z}}(i,j) \ge T_{\bar{\mathbf{z}}} \end{cases} \tag{14}$$

After the stars and noise are further removed, the binary image, the maximum image, and the time-index image are calculated as:

$$\mathbf{B}(i,j) = \overline{\mathbf{b}_{\mathbf{z}}}(i,j)\mathbf{b}_{\bar{\mathbf{z}}}(i,j) \tag{15}$$

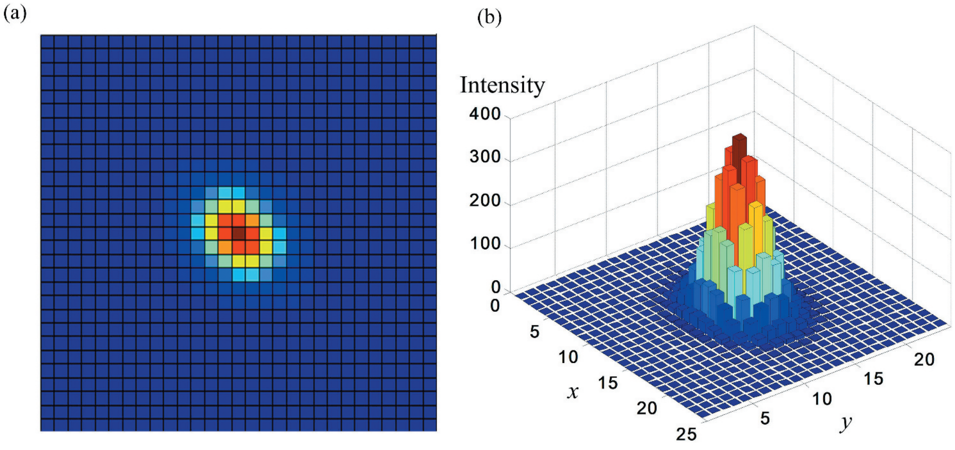

Figure 4. (a) Imaging model of a star, (b) 3D plot of a star.

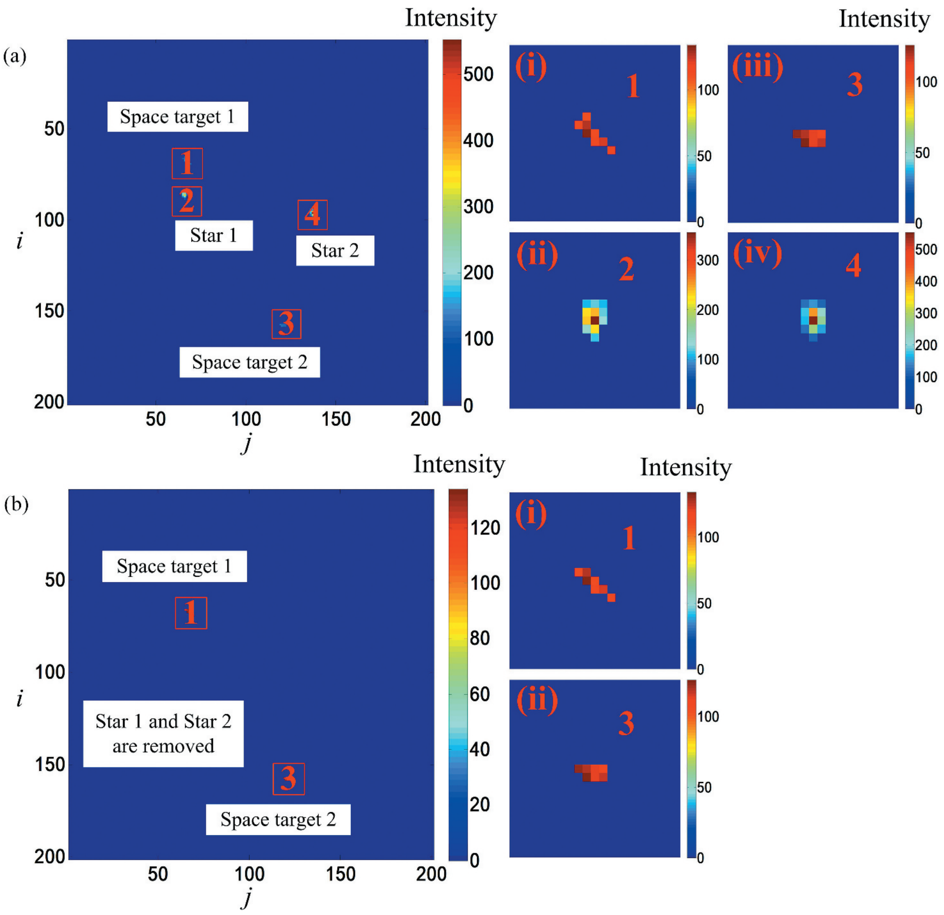

Figure 5. (a) Maximum image after minimum external rectangle detection, (b) maximum image after further removal of bright stars.

$$\mathbf{Z}(i,j) = \mathbf{z}(i,j)\mathbf{B}(i,j) \tag{16}$$

$$\mathbf{T}(i,j) = \mathbf{t}(i,j)\mathbf{B}(i,j) \tag{17}$$

The result is shown in Figure 5, where most of the stars have been removed, leaving only candidate space targets and a few false alarms in the image.

4. Space target detection

4.1. Velocity estimation and state transition

Under the condition involving a long exposure time (3 s), there is obvious movement of the space target in adjacent frames (see Figure 6). The centroid position of the target in the k^{th} frame is $(x(k), y(k))$, the centroid position in the $(k^{\text{th}} + 1)$ frame is $(x(k+1), y(k+1))$, and the distance between the two centroids is $d_{(k,k+1)}$; the distance between the two centroids in the x direction is $d_{x(k,k+1)}$, the distance between

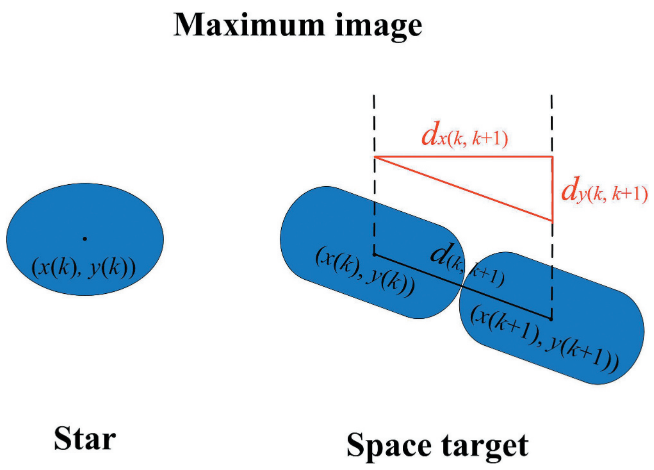

Figure 6. A schematic diagram of the motion relationship between space targets and stars.

the two centroids in the y direction is $d_{y(k,k+1)}$. When the exposure time is t_e and the time interval between two adjacent frames is t_s, the moving speed of the target, which can be used as the basis for selecting the transfer region in the stage involving an allowed state transition, is as follows:

$$v_x = \frac{d_{x(k,k+1)}}{\Delta t} = \frac{x(k+1) - x(k)}{t_\mathrm{e} + t_\mathrm{s}} \tag{18}$$

$$v_y = \frac{d_{y(k,k+1)}}{\Delta t} = \frac{y(k+1) - y(k)}{t_\mathrm{e} + t_\mathrm{s}} \tag{19}$$

The motion of the target can be represented by the following model:

$$\mathbf{x}(k+1) = \mathbf{F}\mathbf{x}(k) \tag{20}$$

$$\mathbf{x}(k) = \begin{bmatrix} x(k) \\ v_x(k) \\ y(k) \\ v_y(k) \end{bmatrix}, \mathbf{F} = \begin{bmatrix} 1 & T & 0 & 0 \\ 0 & 1 & 0 & 0 \\ 0 & 0 & 1 & T \\ 0 & 0 & 0 & 1 \end{bmatrix} \tag{21}$$

where $T = t_\mathrm{e} + t_\mathrm{s}$.

As mentioned above, the target motion model we defined is in the successive state space. However, the detector we have used to capture the image is discrete, and the acquired image is also displayed in a discrete state with the pixel as the basic unit. In addition, predicting the target motion in the discrete state space can reduce the requirement for the target centroid positioning accuracy. Therefore, the state space is quantized. The continuous space is divided into $\Delta \times \Delta$ cells, the size of which is equal to the measurement resolution unit. A discrete state is redefined as: $\overline{\mathbf{x}(k)} = (\overline{x}, \overline{v_x}, \overline{y}, \overline{v_y})$. The relationship between continuous variables and discrete states is shown as:

$$\begin{cases} x(k) \in [(\bar{x} - 1)\Delta, \bar{x}\Delta) \\ y(k) \in [(\bar{y} - 1)\Delta, \bar{y}\Delta) \end{cases} \tag{22}$$

where $1 \leq \bar{x}, \bar{y} \leq N$, and for discrete states, the continuous variables can take any value within the unit.

The velocity space is also divided into $\Delta v \times \Delta v$ cells, where $T\Delta v = \Delta$. In order to ensure the detection probability of space targets with nonlinear trajectories, an improved velocity discrete state is introduced, which is expressed as follows:

$$\begin{cases} v_x(k) \in [(\overline{v_x} - \overline{v_{xx}})\Delta v, (\overline{v_x} + \overline{v_{xx}})\Delta v) \\ v_y(k) \in [(\overline{v_y} - \overline{v_{yy}})\Delta v, (\overline{v_y} + \overline{v_{yy}})\Delta v) \end{cases} \tag{23}$$

where $\overline{v_{xx}}, \overline{v_{yy}}$ are the speed expansion in x and y directions, respectively, representing half of the target search range. The value of $\overline{v_{xx}}$ and $\overline{v_{yy}}$ are $\lceil 0.5\overline{v_x} \rceil$ and $\lceil 0.5\overline{v_y} \rceil$ respectively. The outer parentheses indicate rounding up. The speed dependent adaptive allowed state transitions of the target in the next frame are:

$$\begin{cases} x(k+1) \in [(\bar{x} - 1 + \overline{v_x} - \overline{v_{xx}})\Delta, (\bar{x} + \overline{v_x} + \overline{v_{xx}})\Delta) \\ y(k+1) \in [(\bar{y} - 1 + \overline{v_y} - \overline{v_{yy}})\Delta, (\bar{y} + \overline{v_y} + \overline{v_{yy}})\Delta) \end{cases} \tag{24}$$

This method only needs to search for different orbital altitude targets in the allowed state transition region of each frame (see Figure 7, $\overline{v_{xx}} = 1, \overline{v_{yy}} = 1$). Therefore, this method can effectively detect space targets with different orbital altitudes and nonlinear trajectories, and significantly save computational cost.

4.2. DPSWM algorithm for space target detection

The 3/4 logic of the track initiation sliding window method (used for normal track initiation) is used to detect the space target; namely, the space target is determined when the target appears three times in the candidate trajectory comprising four frames of images. The criteria for determining whether an object is a real space target include:

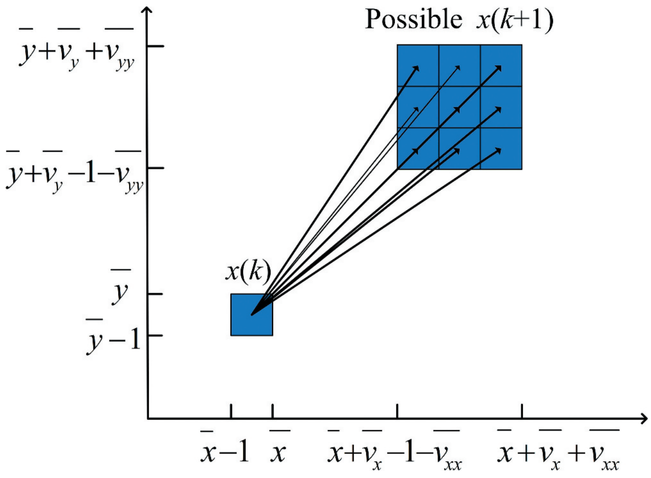

Figure 7. Valid state transitions ($\overline{v_{xx}}= 1, \overline{v_{yy}}= 1$).

(1) A minimum detection criterion: when the number of target points in the candidate trajectory is fewer than the minimum detection number, it cannot be determined as a real space target;
(2) Loss criterion: the target points in candidate trajectories cannot be continuously lost;
(3) Minimum speed criterion: set the minimum speed threshold, and if the candidate target point is lower than that speed, it cannot be identified as a point in the trajectory;
(4) Maximum speed criterion: set the maximum speed threshold, and if the candidate target point is higher than that speed, it cannot be identified as a point in the trajectory.

Of these, the velocity criterion is discussed in section 4.1. Figure 16 lists all forms of real space target trajectories under the above judgement conditions.

where * indicates whether the target is detected (0/1), and this trajectory is a real space target trajectory.

As can be seen from the table, the detection process can be divided into two stages:

Forward detection stage: initiated with the connected regions composed of time indices 1 and 2 in the time-index image $T_{12}(i,j)$ as the root nodes to simultaneously search for the trajectory points with the time indices 3, 4 in the single time-index image;

Reverse detection stage: the real space target determined by the previous step is removed and then initiated with the connected regions composed of time indices 3 and 4 in the time-index image $T_{34}(i,j)$ as the root nodes to simultaneously search for the trajectory points with the time indices 1, 2 in the single time-index image. If the target is not successfully detected in the $T_{12}(i,j)$ image of the previous step, this step can correct the error in time to avoid missing target detection. The forward and reverse bidirectional detection methods ensure the detection probability of space targets with discontinuous trajectories.

The detection steps are shown in Figure 8, where the red line represents the real space target trajectory. P_{12}, P_{34} are the connected regions of the $T_{12}(i,j)$,$T_{34}(i,j)$images, respectively. b_{12}, b_{34} indicate that each connected region contains several frames of image data, and we only continue to detect the connected region containing two frames of image data. P_1, P_2, P_3, P_4 respectively represent the allowed state transition area in each frame image. b_1, b_2, b_3, b_4 denote whether there is a target in the state transition area and, if so, the trajectory is a real target trajectory. 1 means existence, 0 means no.

5. Experiments

In this study, the data acquisition method is the sidereal tracking mode, where the telescope photographs the same area of the sky; in this case, the star is fixed on the focal plane and the space target produces a short line due to the movement. Image processing is undertaken in MATLAB R2014a, and the PC specifications include an i5-3210 M CPU

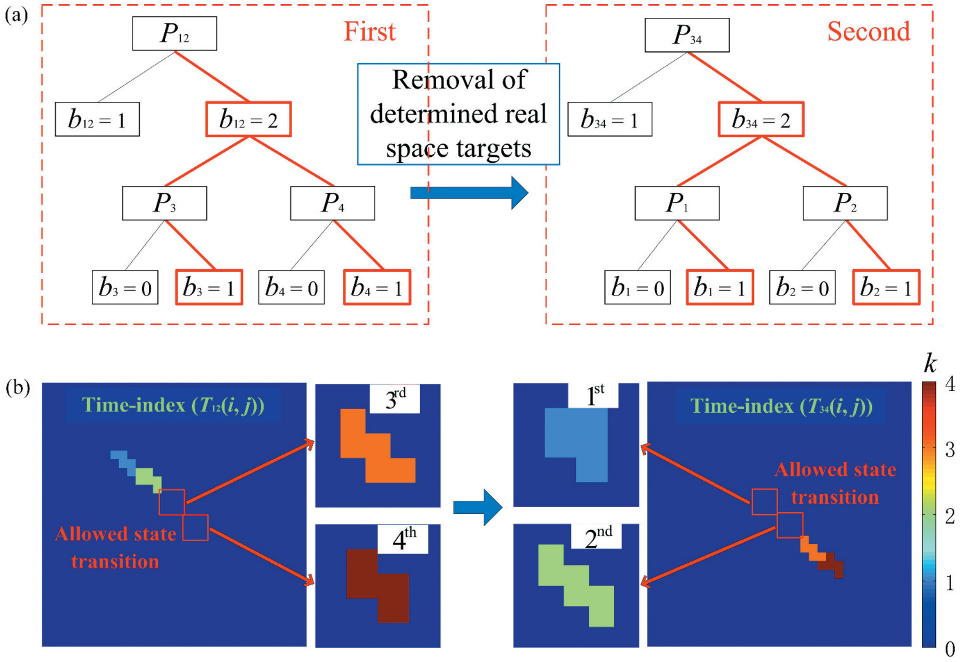

Figure 8. Search tree of DPSWM, (a) frame diagram, (b) time-index image.

(2.50 GHz) with 4 GB of main memory. The image size is 1024 × 1024 pixels. In order to be displayed more clearly, only 512 × 512 pixels are clipped for proof.

The intensity and position of background stars are simulated according to the Tycho-2 catalogue. The space targets with different streak lengths (ranging from 3 to 8) and motion angles are added to 1200 background star images. The 1200 images are divided into four groups, and the SNRs of the space targets in each group are 7, 5, 3, and 1.5. Our algorithm was performed on four sets of images to assess its detection performance. Figure 9 shows the simulated space targets with different streak lengths, motion angles, and the aspect ratio of the minimum external rectangle. Figure 10 shows the simulated space targets with different SNRs.

In order to validate the detection performance of the proposed algorithm, the two indicators used to assess detection performance are detection probability (P_d) and false alarm rate (FAR). The evaluation of these indicators needs to compare the difference between the result of the target detection algorithm and the 'true value', so as to calculate the corresponding indicators. In the simulated image dataset, the detection results of the space targets are compared with the experimental data constructed in the simulation process to validate the correctness of the results. In the real image dataset, the results can be validated by using the information of star list and space debris catalogue. The probability of detection and false alarm rate are calculated from the true target (TT), false target (FT), and missing target (MT).The TT is the number of detected true targets, the FT is the number of false alarms that are misidentified as targets, and the MT is the number of real targets that missing inspection. Based on the above components, the detection probability P_d and false alarm rate FAR are defined as:

(a) Motion angle 0°

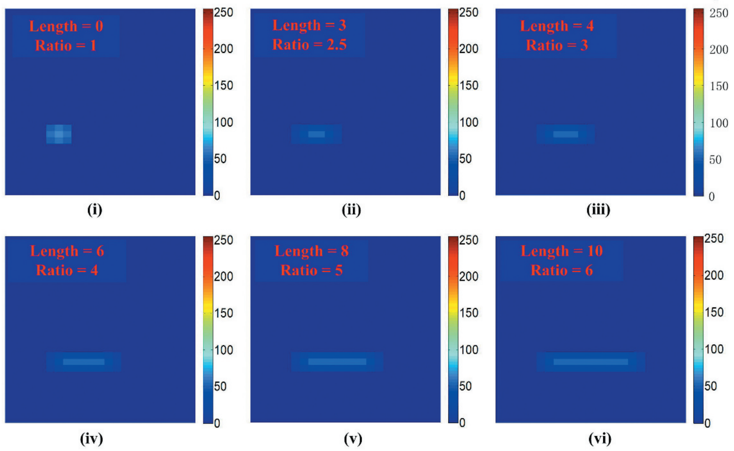

(b) Motion angle 30°

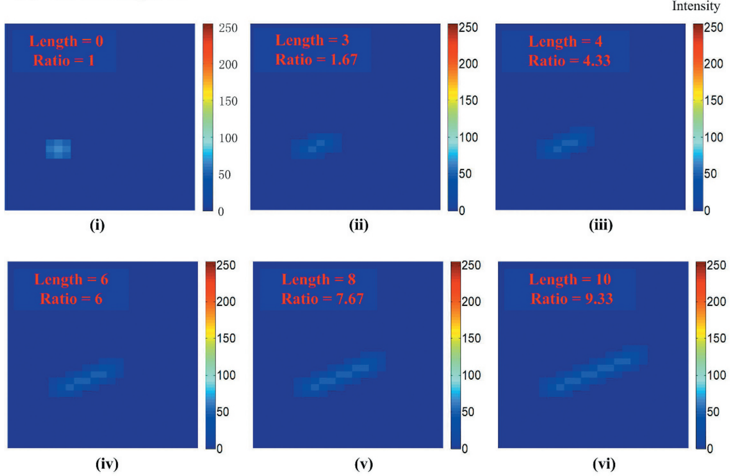

(c) Motion angle 45°

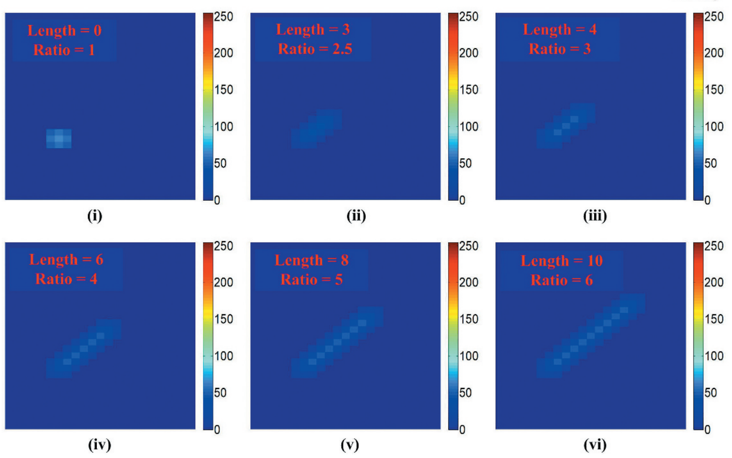

Figure 9. Simulated space targets with different streak lengths and motion angles.

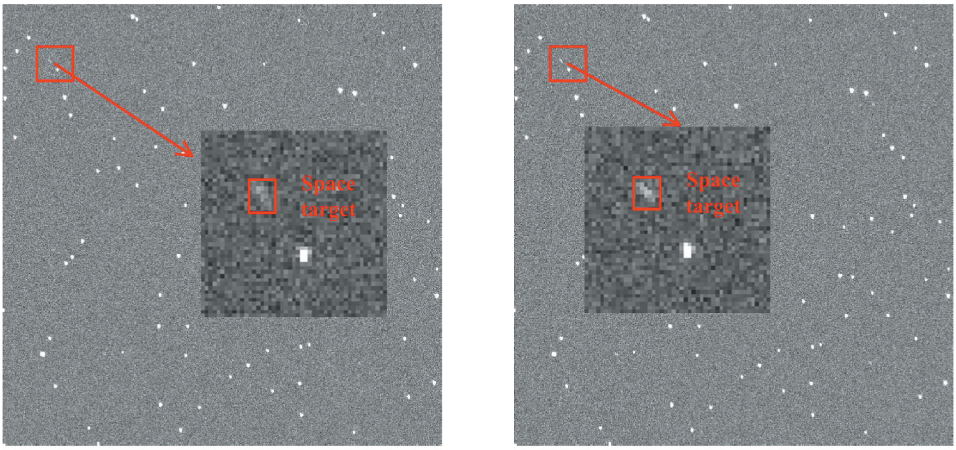

(a) **SNR = 1.5** (b) **SNR = 3**

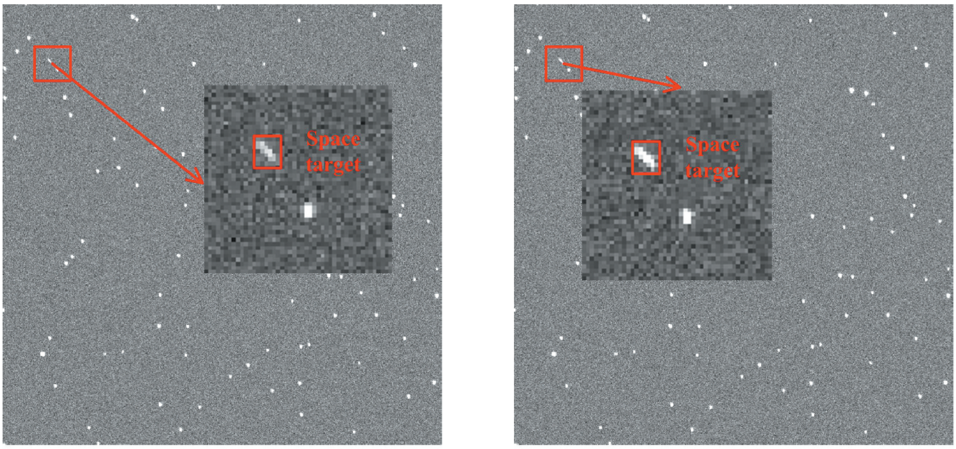

(c) **SNR = 5** (d) **SNR = 7**

Figure 10. Simulated space targets with different SNR.

$$P_{\mathrm{d}} = \frac{(\mathrm{TT})}{(\mathrm{TT}) + (\mathrm{MT})} \tag{25}$$

$$\mathrm{FAR} = \frac{(\mathrm{FT})}{(\mathrm{FT}) + (\mathrm{TT}) + (\mathrm{MT})} \tag{26}$$

5.1. Space target detection using DPSWM

Our DPSWM algorithm was analysed to evaluate its performance in terms of detection and false alarm rejection. The SNR of seven simulated space targets is 3, and two of these are targets entering the field of view. The preliminary test results of the time-index images $T_{12}(i,j)$,$T_{34}(i,j)$ are shown in Figure 11. The light blue connected region in the image represents the object appearing in the first frame, the green represents the second frame, the orange is the third frame, and the red is the fourth frame. Then, DPSWM is used to further detect candidate targets. The results are shown in Figure 12, which represents a binary image and a time index image, respectively. The green circles in the image are the detected real space targets.

For space targets entering the field of view (appearing in the edge area of the image) during the detection process, the target may not always be within the field of view during the four-frame image capture. As shown in Figure 11, the undecided edge targets in Figure 13 appear for the first time in frames 1, 3, 4, and 3, respectively. For such targets, we can continue to make judgements in the next test group. As shown in Figure 13, the undetermined edge points of the first four frames are detected in 5–8 frames. All seven simulated space targets are detected successfully.

The discontinuous and nonlinear situations of the space target trajectories are further tested. Figure 14 shows the detection results.

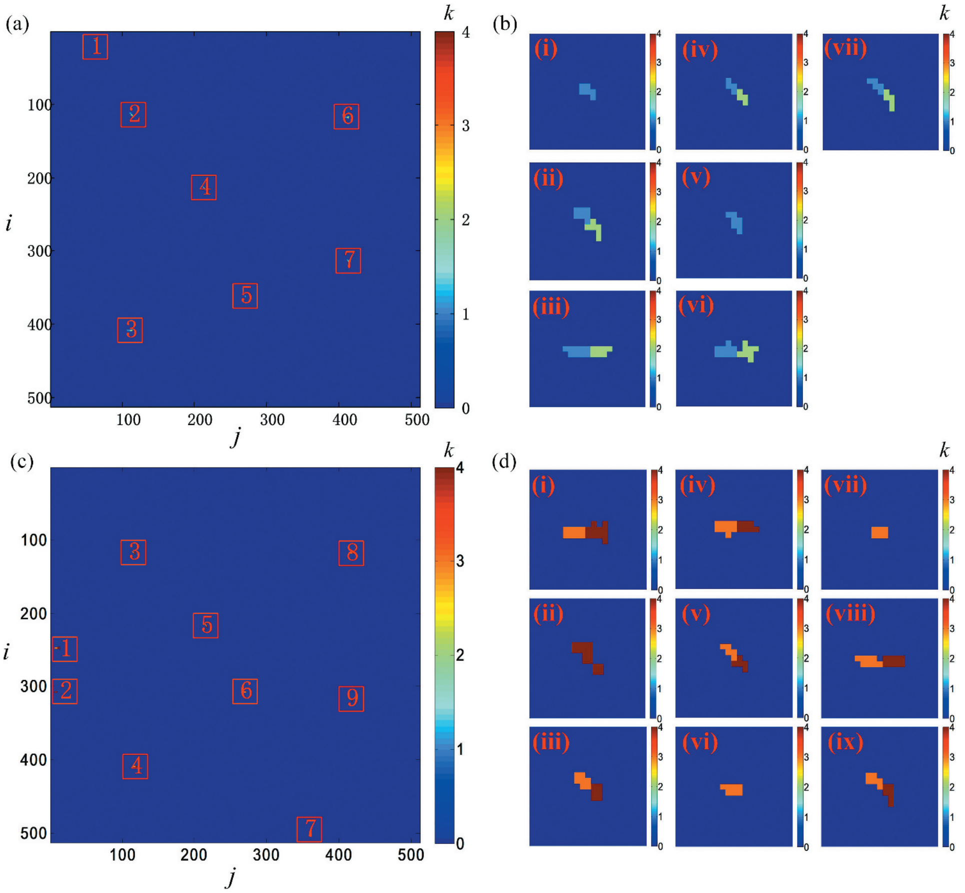

Figure 11. (a) Time-index image after further removal of bright stars (frames 1, 2), (b) enlarged area of the detected candidate targets, (c) time-index image after further removal of bright stars (frames 3, 4), (d) enlarged area of the detected candidate targets.

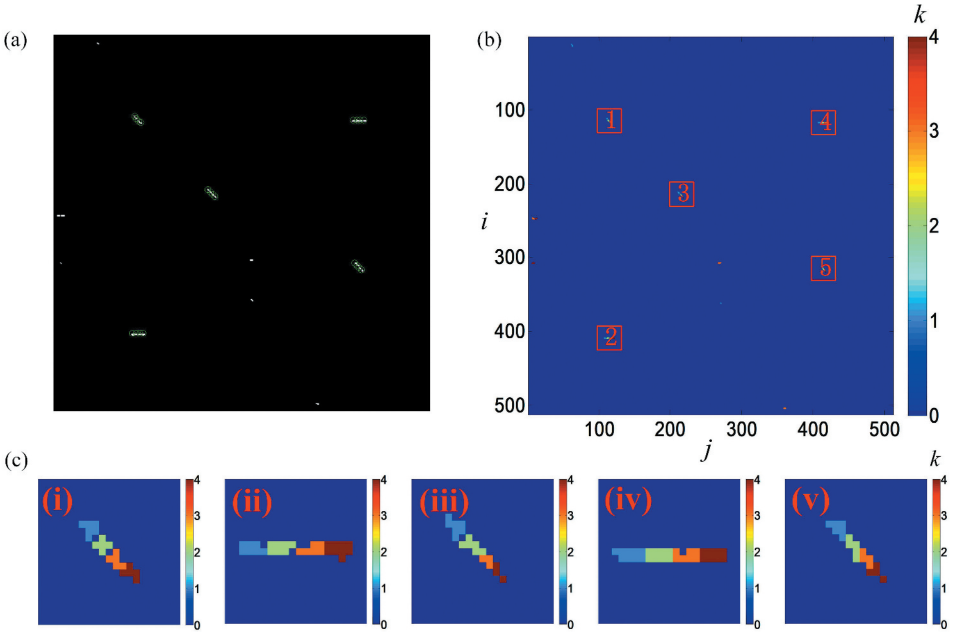

Figure 12. Detection results. (a) binary image, (b) time-index image, (c) enlarged area of the real space targets.

5.2. Real space target detection

The DPSWM method was further performed on real image sets of 500 images to assess its performance in terms of detection and false-alarm rejection. The real images used in the experiments were captured by the CMOS telescope with 3 s exposure time, and have 10240 × 10240 imaging pixels, a 10° × 10° field of view, and 12 bits of greyscale. These images are captured on the ground in the sidereal tracking mode, where the telescope is mounted on a turntable with a velocity to counteract that of the earth's rotation. Space targets appear as streak-like sources. These star images are affected by the vibration of the platform, and some stars also appear as streak-like sources.

In order to validate the effectiveness of the proposed method, DPA (Barniv 1985), IMTI (Yao et al. 2015), and SWM (Worsham 2010) are used to detect the same real image sequences. The statistical results from the different methods are shown in Table 1.

In the DPM method, detection is performed on all possible space target trajectories of the frame set, and the candidate trajectories increase rapidly as the number of target points increases, resulting in a large computational cost. The detection result of the IMTI method is affected by background stars and noise in wide-field surveillance and long exposure times. This method suffers from high false alarm rates, and at least 15 test images were required for space target detection; therefore, 15 images should be stored until the detection process is completed. SWM overcomes the issue of exhaustive searching for all possible space target trajectories by using a sliding window. However, the judging criterion of the method will introduce a high false alarm rate on the premise of ensuring the detection probability.

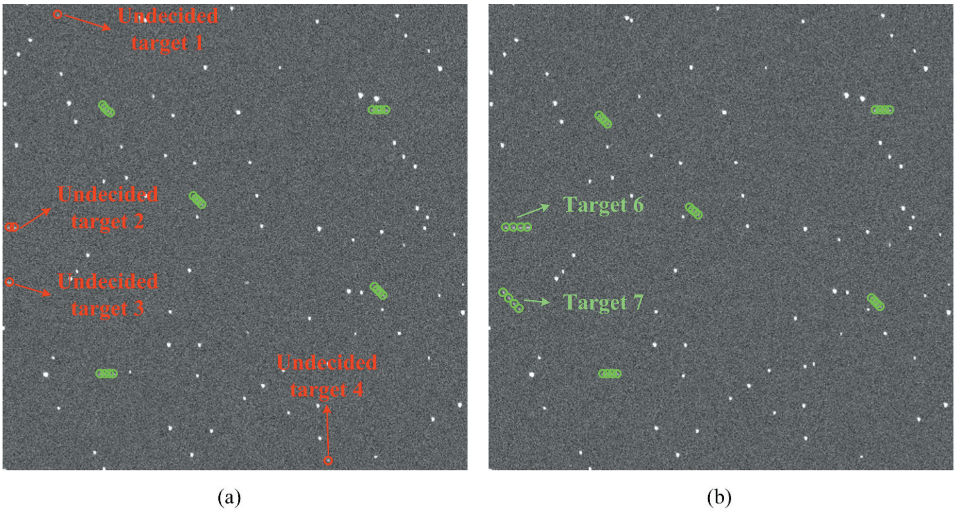

Figure 13. Edge point detection result, (a) (frames 1–4), (b) (frames 5–8).

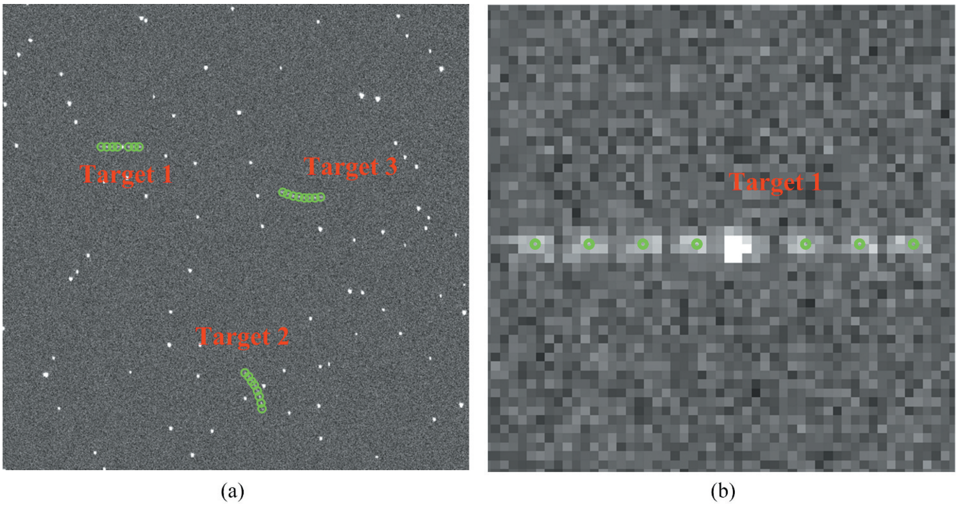

Figure 14. (a) Space target detection results of the discontinuous and nonlinear trajectories with 8 frames, (b) enlarged area of the discontinuous trajectory.

The DPSWM method overcomes the defects of the above method, including a low detection probability and a high false alarm rate due to the interference of stars and noise in the case of wide-field surveillance, long exposure time, and a large computational cost. Partial test results are shown in Figure 15.

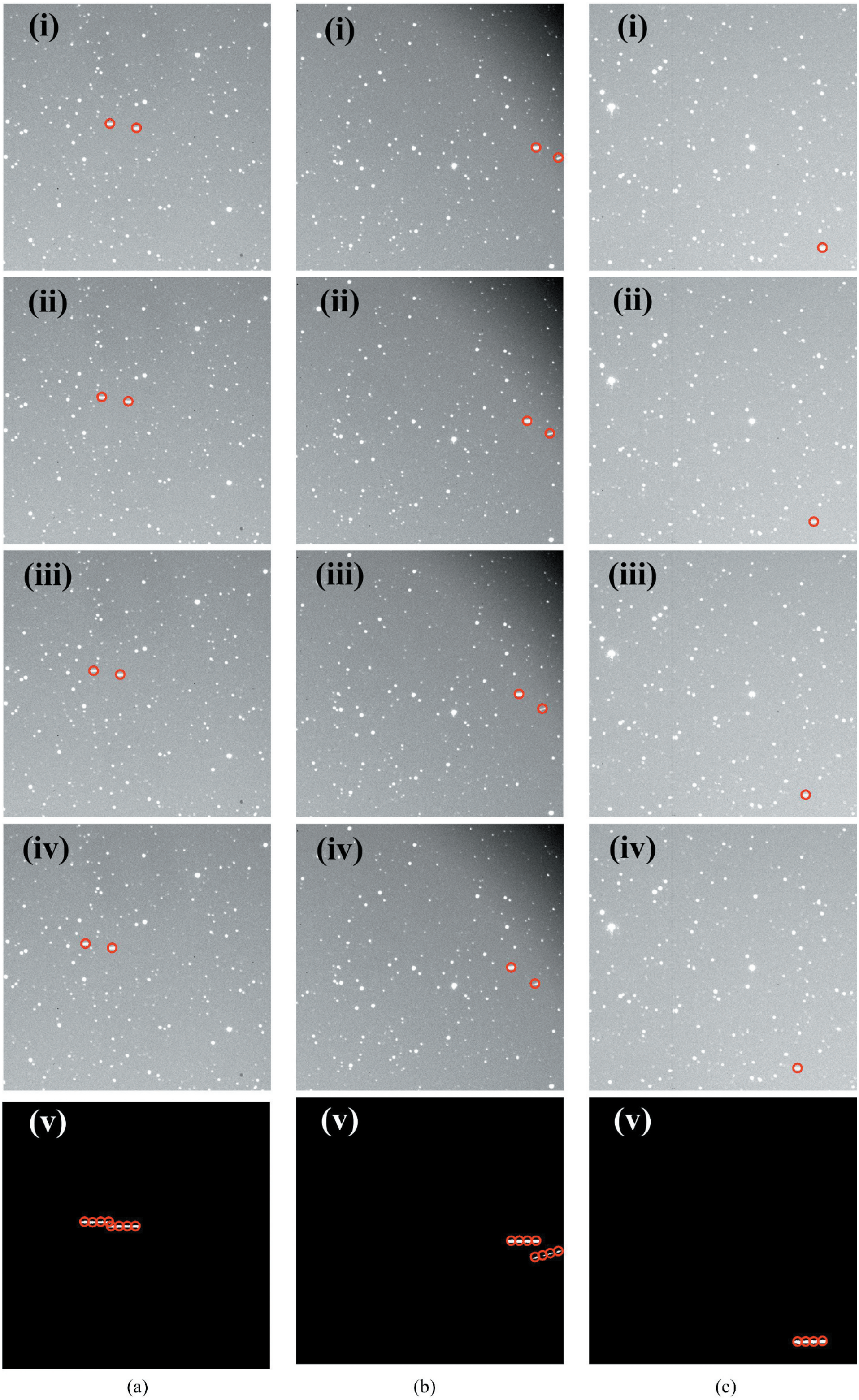

Figure 15. The detection results of the proposed DPSWM in real image sets.

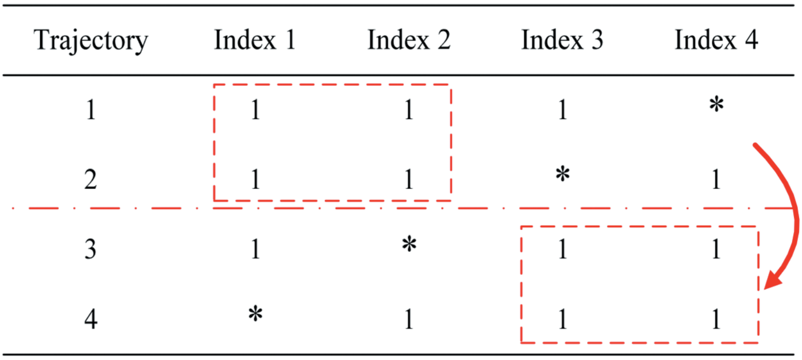

Trajectory	Index 1	Index 2	Index 3	Index 4
1	1	1	1	*
2	1	1	*	1
3	1	*	1	1
4	*	1	1	1

Figure 16. Scores of the real space target trajectories in the time-index image.

Table 1. Statistical results in terms of real space target detection.

Method	Detection probability (%)	False alarm rate (%)	Running time (s)
DPA	88.6	25.6	33.72
IMTI	90.2	15.5	2.85
SWM	92.8	12.3	6.93
DPSWM	98.3	5.4	1.36

6. Conclusions

In this paper, a method for space target detection in wide-field surveillance is proposed. Under the condition of a wide field of view and long exposure time, the number of object points is numerous, and some stars manifest as streak-like sources. The proposed minimum external rectangle method can effectively eliminate stars and noise. As opposed to applying this method to a single image, the application in the time index image can remove more background points by increasing the *R* threshold. After removing background stars and noise, the allowed state transition region in each image of the frame set is predicted. The improved velocity discrete state can ensure the detection probability of space targets with nonlinear trajectories, and the speed dependent adaptive allowed state transition region can effectively detect space targets with different orbital altitudes. Subsequently, the DPSWM method is performed to detect space targets, and the forward and reverse bidirectional detection methods ensure the detection probability of space targets with discontinuous trajectories. The experimental results show that the proposed method has a high detection accuracy and low computational cost to overcome the obstacles of space target detection in wide-field surveillance under long exposure times.

Disclosure statement

No potential conflict of interest was reported by the authors.

Funding

This work was supported by the [Strategic Priority Research Program of Chinese Academy of Sciences] under Grant [No. XDA17010205]

References

Ahmadi, K., and E. Salari. 2015. “Small Dim Object Tracking Using A Multi Objective Particle Swarm Optimisation Technique.” *IET Image Processing* 9 (9): 820–826. doi:10.1049/iet-ipr.2014.0927.

Arnold, J., S. W. Shaw, and H. Pasternack. 1993. “Efficient Target Tracking Using Dynamic Programming.” *IEEE Transactions on Aerospace and Electronic Systems* 29 (1): 44–56. doi:10.1109/7.249112.

Bai, X. 2013. “Morphological Operator for Infrared Dim Small Target Enhancement Using Dilation and Erosion through Structuring Element Construction.” *Optik* 124 (23): 6163–6166. doi:10.1016/j.ijleo.2013.04.098.

Bai, X., F. Zhou, Y. Xie, and T. Jin. 2009. “Enhanced Detect Ability of Point Target Using Adaptive Morphological Clutter Elimination by Importing the Properties of the Target Region.” *Signal Process* 89: 1973–1989.

Barniv, Y. 1985. “Dynamic Programming Solution for Detecting Dim Moving Targets.” *IEEE Transactions on Aerospace and Electronic Systems* 21 (1): 144–156. doi:10.1109/taes.1985.310548.

Blostein, S. D., and T. S. Huang. 1991. “Detecting Small, Moving Objects in Image Sequences Using Sequential Hypothesis Testing.” *IEEE Transactions on Signal Processing* 39 (7): 1611–1629. doi:10.1109/78.134399.

Blostein, S. D., and H. S. Richardson. 1994. “A Sequential Detection Approach to Target Tracking.” *IEEE Transactions on Aerospace and Electronic Systems* 30 (1): 197–212. doi:10.1109/7.250420.

Castronuovo, M. M. 2011. “Active Space Debris Removal-A Preliminary Mission Analysis and Design.” *Acta astronautica* 69 (9–10): 848–859. doi:10.1016/j.actaastro.2011.04.017.

Chen, Y. 2019. “Infrared Small Target Detection through Multiple Feature Analysis Based on Visual Saliency.” *IEEE Access* 7: 38996–39004. doi:10.1109/ACCESS.2019.2906076.

Chu, P. L. 1988. “Optimal Projection for Multidimensional Signal Detection.” *IEEE Transactions on Acoustics, Speech, and Signal Processing* 36 (5): 775–786. doi:10.1109/29.1587.

Chu, P. L. 1989. “Efficient Detection of Small Moving Objects.” *MIT Lincoln Laboratory Technical Report*, 35–41.

Dong, X., X. Huang, Y. Zheng, S. Bai, and W. Xu. 2014. “A Novel Infrared Small Moving Target Detection Method Based on Tracking Interest Points under Complicated Background.” *Infrared Physics and Technology* 65 (2014): 36–42. doi:10.1016/j.infrared.2014.03.007.

Esmiller, B., C. Jacquelard, H. Eckel, and E. Wnuk. 2014. “Space Debris Removal by Ground-Based Lasers: Main Conclusions of the European Project: CLEANSPACE.” *Applied Optics* 53 (31): 145–154. doi:10.1364/ao.53.000i45.

Gao, J., Z. Lin, and W. An. 2019. “Infrared Small Target Detection Using a Temporal Variance and Spatial Patch Contrast Filter.” *IEEE Access* 7: 32217–32226.

Johnston, L. A., and V. Krishnamurthy. 2000. “Performance Analysis of a Track before Detect Dynamic Programming Algorithm.” *IEEE International Conference on Acoustics, Speech, and Signal Processing, Istanbul*, 49–52. doi:10.1109/ICASSP.2000.861860

Kravchonok, A. 2011. “Detection of Moving Objects in Video Sequences by the Computation of Optical Flow Based on Region Growing.” *Pattern Recognition and Image Analysis* 21 (2): 283–286. doi:10.1134/S1054661811020647.

Li, M., C. Yan, C. Hu, C. Liu, and L. Xu. 2019. “Space Target Detection in Complicated Situations for Wide-Field Surveillance.” *IEEE Access* 7: 123658–123670. doi:10.1109/ACCESS.2019.2938454.

Liu, R., X. Li, L. Han, and J. Meng. 2013. “Track Infrared Point Targets Based on Projection Coefficient Templates and Non-Linear Correlation Combined with Kalman Prediction.” *Infrared Physics and Technology* 57: 68–75. doi:10.1016/j.infrared.2012.12.011.

Liu, R., Y. Lu, C. Gong, and Y. Liu. 2012. "Infrared Point Target Detection with Improved Template Matching." *Infrared Physics* 55 (4): 380–387. doi:10.1016/j.infrared.2012.01.006.

Mehrholzet, D., L. Leushacke, and W. Flury. 2002. "Detecting, Tracking and Imaging Space Debris." *Bulletin. Bulletin European Space Agency* 109 (109): 128–134. doi:10.2514/2.1656.

Nunez, J., A. Nunez, F. J. Montojo, and M. Condominas. 2015. "Improving Space Debris Detection in GEO Ring Using Image Deconvolution." *Advances in Space Research* 56 (2): 218–228. doi:10.1016/j.asr.2015.04.006.

Reed, I. S., R. M. Gagliardi, and L. B. Stotts. 1990. "A Recursive Moving-Target-Indication Algorithm for Optical Image Sequences." *IEEE Transactions on Aerospace and Electronic Systems* 26 (3): 434–440. doi:10.1109/7.106120.

Sease, B., B. Flewelling, and J. Black. 2017. "Automatic Streak Endpoint Localization from the Cornerness Metric." *Acta astronautica* 134: 345–354.

Tonissen, S. M., and R. J. Evans. 1996. "Performance of Dynamic Programming Techniques for Track-Before-Detect." *IEEE Transactions on Aerospace and Electronic Systems* 32 (4): 1440–1451. doi:10.1109/7.543865.

Wei, M., F. Xing, and Z. You. 2018. "A Real-Time Detection and Positioning Method for Small and Weak Targets Using A 1D Morphology-Based Approach in 2D Images." *Light: Science & Applications* 7 (3): 97–106. doi:10.1038/lsa.2018.6.

Wirnsberger, H., O. Baur, and G. Kirchner. 2015. "Space Debris Orbit Prediction Errors Using Bi-Static Laser Observations. Case Study: ENVISAT." *Advances in Space Research* 55 (11): 2607–2615. doi:10.1016/j.asr.2015.02.018.

Worsham, R. 2010. "The Probabilities of Track Initiation and Loss Using a Sliding Window for Track Acquisition." *Proc. IEEE Radar Conference*, Baltimore, 1270–1275. doi:10.1109/RADAR.2010.5494424.

Xi, J., D. Wen, O. K. Ersoy, H. Yi, D. Yao, Z. Song, and S. Xi. 2016. "Space Debris Detection in Optical Image Sequences." *Applied Optics* 55 (28): 7929–7940. doi:10.1364/AO.55.007929.

Xu, W., Q. Li, H. Feng, Z. Xu, and Y. Chen. 2013. "A Novel Star Image Thresholding Method for Effective Segmentation and Centoid Statistics." *Optik* 124 (20): 4673–4677. doi:10.1016/j.ijleo.2013.01.067.

Yang, Y., and H. Lin. 2010. "Automatic Detecting and Tracking Space Debris Objects Using Active Contours from Astronomical Images." *Geomatics & Information Science of Wuhan University* 35 (2): 209–214.

Yao, D., D. Wen, J. Xue, Z. Chen, and Y. Wen. 2015. "Maximum Projection and Velocity Estimation Algorithm for Small Moving Target Detection in Space Surveillance." *Image Processing and Analysis* 96752H. doi:10.1117/12.2202360.

Zhang, T., C. Cui, W. Fu, H. Huang, and H. Cheng. 2018. "Improved Small Moving Target Detection Method in Infrared Sequences under A Rotational Background." *Applied Optics* 57: 9279–9286. doi:10.1364/AO.57.009279.